Ultramicroscopy 143 (2014) 77–87

Contents lists available at ScienceDirect

Ultramicroscopy

journal homepage: www.elsevier.com/locate/ultramic

Imaging endosomes and autophagosomes in whole mammalian cells using correlative cryo-fluorescence and cryo-soft X-ray microscopy (cryo-CLXM)

Elizabeth M.H. Duke [a,1], Minoo Razi [b,1], Anne Weston [c], Peter Guttmann [d], Stephan Werner [d], Katja Henzler [d], Gerd Schneider [d], Sharon A. Tooze [b], Lucy M. Collinson [c,*]

[a] Diamond Light Source, Harwell Science and Innovation Campus, Didcot, Oxfordshire OX11 0DE, UK
[b] Secretory Pathways Laboratory, London Research Institute, Cancer Research UK, London WC2A 3LY, UK
[c] Electron Microscopy Unit, London Research Institute, Cancer Research UK, London WC2A 3LY, UK
[d] Helmholtz-Zentrum Berlin für Materialien und Energie GmbH, Institute for Soft Matter and Functional Materials, 12489 Berlin, Germany

ARTICLE INFO

Available online 21 October 2013

Keywords:
Cryo-fluorescence
Cryo-soft X-ray tomography
Cryo-CLXM
Endosomes
Autophagosomes
Omegasomes

ABSTRACT

Cryo-soft X-ray tomography (cryo-SXT) is a powerful imaging technique that can extract ultrastructural information from whole, unstained mammalian cells as close to the living state as possible. Subcellular organelles including the nucleus, the Golgi apparatus and mitochondria have been identified by morphology alone, due to the similarity in contrast to transmission electron micrographs. In this study, we used cryo-SXT to image endosomes and autophagosomes, organelles that are particularly susceptible to chemical fixation artefacts during sample preparation for electron microscopy. We used two approaches to identify these compartments. For early and recycling endosomes, which are accessible to externally-loaded markers, we used an anti-transferrin receptor antibody conjugated to 10 nm gold particles. For autophagosomes, which are not accessible to externally-applied markers, we developed a correlative cryo-fluorescence and cryo-SXT workflow (cryo-CLXM) to localise GFP-LC3 and RFP-Atg9. We used a stand-alone cryo-fluorescence stage in the home laboratory to localise the cloned fluorophores, followed by cryo-soft X-ray tomography at the synchrotron to analyse cellular ultrastructure. We mapped the 3D ultrastructure of the endocytic and autophagic structures, and discovered clusters of omegasomes arising from 'hotspots' on the ER. Thus, immunogold markers and cryo-CLXM can be used to analyse cellular processes that are inaccessible using other imaging modalities.

1. Introduction

Correlative Light and Electron Microscopy (CLEM) is a powerful tool for identifying the subcellular localisation of fluorescent proteins within the reference space of the cell [1]. CLEM has been successfully applied to many studies of membrane trafficking in mammalian cells, including those involving the endocytic [2,3], recycling [4,5], secretory [6–8] and autophagy pathways [9–11]. However, the multi-stage sample preparation process has drawbacks. Chemical fixatives penetrate the sample too slowly to instantaneously preserve dynamic structures, heavy metal stains mask the atomic composition of the cell and dehydration of the specimen can cause deformation of the membranes. In addition, many consecutive (serial) sections must be cut, collected, imaged and reconstructed for 3D analysis of complex organelles.

Cryo-preservation techniques including plunge freezing (for samples less than 10 μm thick) and high pressure freezing (HPF; for samples less than 200 μm thick) are fast and circumvent the need for chemical fixatives, giving optimal sample preservation. Frozen samples may then be freeze-substituted into resin and observed at ambient temperature in a TEM (transmission electron microscope), or imaged directly at cryo-temperatures using

Abbreviations: CEMOVIS, Cryo-Electron Microscopy of Vitreous Sections; CLEM, Correlative Light and Electron Microscopy; Cryo-CLXM, Cryo-Correlative Light and X-ray Microscopy; Cryo-SXT, cryo-Soft X-ray Tomography; Cryo-TEM, cryo-transmission electron microscopy; ER, endoplasmic reticulum; FIB, Focused Ion Beam; GFP, Green Fluorescent Protein; HPF, high pressure freezing; PNR, perinuclear region; RFP, Red Fluorescent Protein; TfnR, transferrin receptor; VTC, vesicular–tubular clusters

* Corresponding author. Tel.: +44 207 269 3416.
E-mail address: lucy.collinson@cancer.org.uk (L.M. Collinson).
[1] Joint first authors.

0304-3991
http://dx.doi.org/10.1016/j.ultramic.2013.10.006

cryo-TEM, thus avoiding shrinkage artifacts caused by dehydration. However, sample thickness is limited to around 1 μm in a 300 kV TEM due to the penetration of the electron beam. Whereas studies of thin peripheral regions of intact cells are possible [12], studies of the thicker perinuclear region (PNR) in intact cells are not. Cryo-Electron Microscopy of Vitreous Sections (CEMOVIS) [13] or Focused Ion Beam (FIB) milling [14] can be used to view sections cut through the thicker perinuclear region (PNR) of frozen cells, which contains many of the cell's organelles, but imaging through an entire cell by either technique would be near-impossible.

Synchrotron-hosted cryo-soft X-ray tomography (cryo-SXT) is an emerging technique that allows imaging of unstained, cryo-preserved biological samples as close to their native state as possible [15–17]. Cells may be loaded into capillaries [18] or grown on carbon-coated grids [19,20]. Samples are then prepared by plunge-freezing, or more recently by HPF [21], both of which are highly effective at preserving dynamic and volatile cellular structures. Samples are then imaged in a cryo-SXT microscope at one of three synchrotron beamlines currently operational worldwide (the Advanced Light Source in the USA, BESSY II in Germany, ALBA in Spain). Image contrast is due to differential, quantitative absorption of X-ray photons in the 'water window', between the K-shell absorption edges of carbon (284 eV) and oxygen (543 eV) [19]. Here, organic materials show strong absorption and phase contrast, whereas water is relatively non-absorbing [22,23]. Fortuitously, at this energy, the X-rays penetrate through ~10 μm of ice. Therefore, whole mammalian cells can be imaged at near-native state, without chemical fixation, staining or sectioning.

Cryo-SXT has been applied to a range of sample types including yeast cells [24–28], mammalian cells [16,17,29–31] and virus-infected cells [20,32,33]. Ultrastructural preservation is similar to cryo-TEM of thin regions of frozen-hydrated cells [12] with the additional advantage of being able to image through the thickest part of the cell. Contrast is similar to TEM images of heavy-metal stained and resin-embedded cells, enabling identification of organelles including the nucleus, mitochondria, the Golgi apparatus and endoplasmic reticulum (ER) by their characteristic morphology [31]. However, organelles that may require immunogold labelling or CLEM for unambiguous identification in TEM, including endosomes and autophagosomes, have not yet been characterised in cryo-SXT images.

Recently, correlative studies combining cryo-fluorescence microscopy with cryo-SXT have started to link function to native-state ultrastructure, using either a cryogenic light microscope prior to cryo-SXT imaging [34–36], or a fluorescence microscope inside the X-ray microscope itself [19,20]. Here we report the use of a stand-alone cryo-fluorescence stage [37], which can be mounted on any standard widefield epifluorescence light microscope, for identification of fluorophore-labelled organelles using correlative cryo-fluorescence and cryo-soft X-ray microscopy (cryo-CLXM). We used cryo-CLXM to characterise structures of the endocytic and early autophagy pathway. Early autophagosomes can be difficult to localise, even using CLEM, as they are particularly susceptible to chemical fixation artifacts [38,39] and so would specifically benefit from a cryo-preparation and cryo-imaging approach.

To remain healthy, eukaryotic cells require a constant turnover and replacement of old components with functional new ones. Disposing of old organelles is a challenging task that cells tackle with autophagy, a lysosome-mediated degradative pathway. A key event in autophagy is the formation of a double-membrane structure called an autophagosome, which engulfs portions of cytosol and entire organelles. Autophagosome formation can be divided into five steps (with structure): induction (the pre-autophagosomal structure), expansion (the phagophore and the omegasome), vesicle completion (the autophagosome), fusion with the endo-lysosomal system (the amphisome) and cargo degradation by lysosomal enzymes (the autolysosome/lysosome) [40]. Autophagy specific proteins, called "Atg" proteins in yeast, can be used as markers for different stages of autophagosome formation. Atg9 is the only known transmembrane protein involved and is essential for the formation of early autophagosomal structures [41] whereas LC3 (Atg8) is cytosolic and is recruited to forming autophagosomes. Immunogold labelling [42] and CLEM revealed that Atg9 localises to complex vesicular–tubular clusters surrounding electron-lucent endosome-like organelles (Atg9-VTC) that interact with transferrin-receptor-positive endosomes [40]. However, despite fluorescence data indicating that Atg9-VTC co-locate with LC3-positive membranes, recognisable early autophagosomal structures were difficult to find and so our understanding of the early autophagy pathway remains incomplete.

In order to characterise forming autophagosomes in the vicinity of Atg9-VTC and endosomes, we developed a workflow for cryo-CLXM and also loaded the cells with an endosome-specific gold marker. We imaged co-localised RFP-Atg9 and GFP-LC3 signals in vitrified Hek293 cells using benchtop cryo-fluorescence microscopy, which also allowed us to screen samples for areas of suitable ice thickness. Using the HZB cryo full-field transmission X-ray microscope installed at the U41 beamline at the BESSY II electron storage ring (Berlin, Germany), we collected tomograms from the regions of interest in whole, unstained Hek293 cells. We identified early and recycling endosomes using an anti-transferrin receptor antibody conjugated to 10 nm gold particles (anti-TfnR-gold). Using our correlative workflow, we identified LC3-positive membranes that we postulate are omegasomes [43] due to their cup-shaped morphology. The omegasomes co-locate with TfnR-positive endosomes and Atg9-VTC, and for the first time we show multiple omegasomes arising in clusters from the same ER subdomain. Thus, cryo-CLXM and immunogold labelling can be used to identify the morphology of subcellular compartments close to their native-state, and reveal structure–function information about subcellular processes that are difficult to capture using traditional imaging techniques.

2. Materials and methods

2.1. Cells and constructs

The HEK293A/GFP-LC3/mRFP-Atg9 cells were previously described [10]. Cells were maintained in full medium (FM): DMEM with 10% foetal calf serum (FCS) as previously described [44,45]. To induce autophagy, cells were incubated for 2 h in starvation medium (Earle's balanced salt solution, EBSS). For identification of endocytic compartments, anti-TfnR-gold conjugate (10-nm gold) was added to the EBSS.

2.2. Holey carbon film preparation

HZB-2 gold grids (Gilder Grids, UK) were coated with holey-carbon films as a support for cell growth. Grids coated with 2/2 Quantifoil® film (Quantifoil, Germany) allowed uniform blotting prior to plunge freezing, and the holes were also found to be particularly useful for alignment during data reconstruction and correlation between imaging modalities. However, due to the expense and time taken to produce these grids, homemade films were also used. To make these, 20 drops of a 1:1 glycerol:dd H_20 solution were added to 50 ml of 0.5% (w/v) formvar in chloroform. The mixture was shaken vigorously for 30 s to disperse the aqueous glycerol into the solvent, and then sonicated using a microprobe sonicator for 60 s at 50% power, to reduce the glycerol microdroplet size. The solution was immediately transferred to a

coplin jar and slides were dipped into the solution and removed at constant speed. Film-coated slides were allowed to dry in a humid atmosphere prior to floating the films onto water. HZB-2 grids were placed onto the film and picked up onto glass slides. Holey formvar films were checked in a Tecnai G2 Spirit 120 kV transmission electron microscope (FEI Company) with an Orius CCD camera (Gatan Inc.) for size and distribution. Grids were released from the slide and etched for 10 min with methanol to remove glycerol and sharpen the hole edges. The grids were then coated with 5–10 nm carbon in a MED020 high resolution coater (Leica Microsystems UK) and the formvar film removed by incubation on 1,2-dichloroethane for 2 h.

2.3. Sample preparation for cryo-soft X-ray microscopy

HZB-2 grids were glow-discharged and a thin line of liquid blocker (PAP pen) was placed next to the observation region of the grid [20]. Grids were placed into cell growth medium in 12-well dishes and cells were seeded and allowed to settle overnight. A confluency of about 50% ensured that cells were sparse enough that they would not overlap at high tilt during cryo-SXT data collection.

Immediately prior to freezing, grids were blotted from the rear using Whatman filter paper no.4 to remove excess medium, and 1.75 µl of an aqueous solution containing 250 nm gold particles was added to the grid tip for use as fiducial markers (BBI). Grids were then plunge frozen in a Vitrobot Mk IV (FEI Company). Briefly, grids were clamped into Vitrobot tweezers taking care that the tweezer tips remained below the PAP-pen line. The tweezers were placed into the plunge freezer, held at 70% relative humidity and 37 °C. The grid was manually blotted from behind using Whatman no.4 filter paper, and the grid was plunge frozen in liquid nitrogen-cooled liquid ethane. Grids were transferred to 2 ml cryotubes and stored in cryocanes under liquid nitrogen.

2.4. Cryo-fluorescence microscopy

Grids were transferred under liquid nitrogen to the cold-stage grid holder, which was modified from the original 3 mm grid design for cryo-electron microscopy [37] to accommodate the HZB-2 grids (by Linkam Scientific Instruments, Epsom, UK; Fig. 1b,c). The grid holder was inserted into a cryo-stage (Linkam Scientific Instruments, Epsom, UK) on an Axio Scope A1m epi-fluorescence microscope fitted with an AxioCam CCD (Carl Zeiss Ltd, Oxfordshire, UK). The grids were imaged at −160 °C. Each grid slot was imaged, assessed and mapped for ice thickness. Although ice thickness could not be accurately quantified in the light microscope, thickness could be estimated based on cell morphology (over−blotting leads to thin ice and disrupted cell morphology) and image quality (under-blotting leads to thick ice, causing scattering of light, leading to reduced fluorescence intensity and poor focus). Cells embedded in areas of optimal ice thickness were further screened for co-expression of RFP-Atg9 and LC3-GFP, whilst discarding areas with cracks in the ice, ice contamination, tears in the carbon film, or areas close to grid bars that would

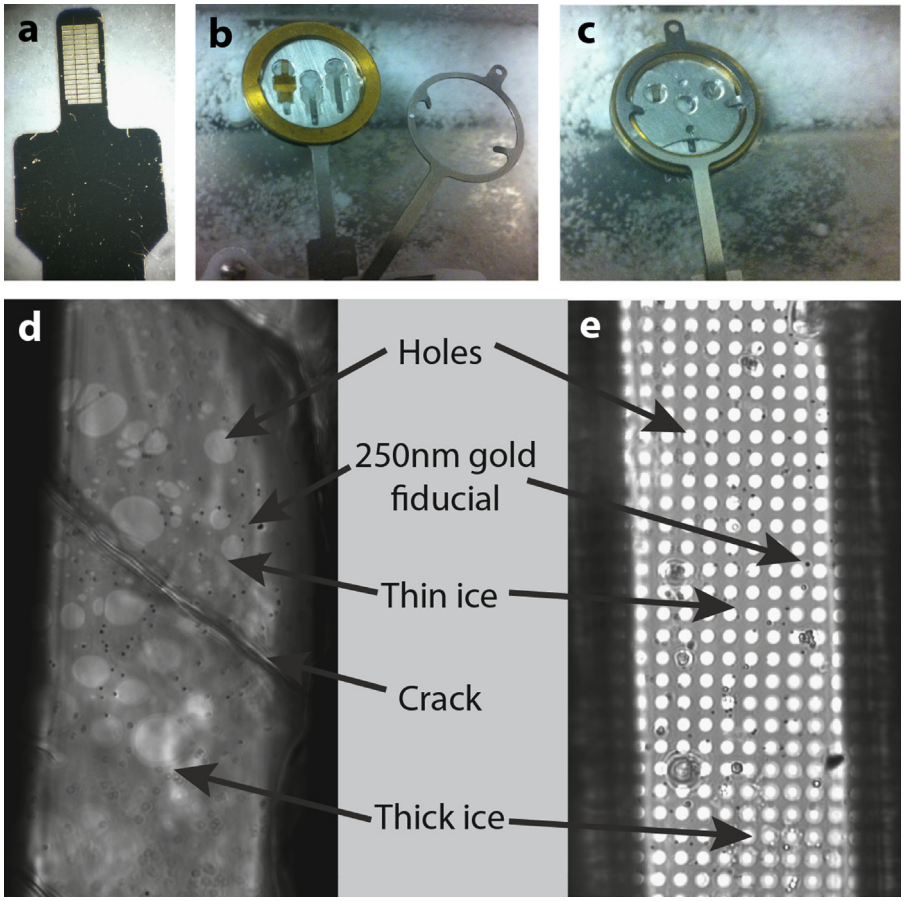

Fig. 1. Sample preparation for cryo-SXT of vitrified Hek293 cells. Grids were imaged using a Zeiss AxioScope with a cryo-stage cooled to −160 °C. The HZB-2 grids (a) were placed into a modified grid holder under liquid nitrogen (b) and clamped into place (c). Cryo-brightfield microscopy of homemade (d) and Quantifoil® (e) holey-carbon films demonstrated that the 250 nm gold fiducials and holes in the carbon film can be easily seen and can thus be used as correlation markers for cryo-SXT. In addition, cryo-brightfield imaging detects artefacts including cracks in the ice, debris, and thick ice, which can be mapped and avoided in the X-ray microscope.

block images at high tilt angles. After imaging, grids were returned to liquid nitrogen storage.

2.5. Cryo-soft X-ray tomography

Grids were transferred to the BESSY II electron storage ring (Berlin, Germany) in a dry nitrogen shipper. Grids were loaded into a Gatan 630 cryo holder and inserted into the FEI compustage for imaging by cryo-SXT at cryogenic temperatures as previously described [17]. Cells of interest were efficiently relocated using the cryo-fluorescence maps and imaged using the in-vacuum fluorescence microscope as previously described [20]. For these experiments, focus was set using the nuclear envelope. Between 96 and 126 projection images were collected for each tilt series at 1° increments (depending on the maximum possible tilt angle for each cell, taking into account grid bars, adjacent cells and sample thickness at high tilt angles) at 2.43 nm wavelength (photon energy $E=510$ eV) with a 40 nm zone plate and an image pixel size of 15.5755 nm. Data collection procedure followed a very similar pattern to that reported in [20] with one notable and significant exception. As a result of previous experience on another project (unpublished work) where irreversible damage was seen during the course of tomographic data collection, a low dose approach was adopted for data collection. The exposure time per image was set such that the maximum number of counts in the image at 0° was from ~6000 to 7000 (detector saturation level ~65,000). This ensured that no structural alteration as judged by eye could be seen between the two 0° images collected as controls before and after the tilt series data collection.

2.6. Data analysis

An average flat field was calculated from 10 flat field images for each tilt series, which was used to normalise each image in the tilt series. Tomographic reconstruction was performed using the eTomo workflow in IMOD [46]. The 250 nm gold fiducials were used for manual image alignment. Great care was taken to ensure that the centre of each fiducial was chosen with automated positioning, refined by hand if necessary. Residual differences between frames in IMOD obtained in the X-ray data are similar to those experienced when processing cryo-EM data (which uses much smaller fiducial markers) due to the high level of contrast in each individual image. Linear interpolation was used with an aligned image stack binning of 2. A tomogram thickness of around 1200 was selected, with a Radial Filter Cutoff of 0.3 and a Falloff of 0.065. Both back projection and SIRT reconstructions (15 iterations) were performed for each dataset. Resulting image stacks were saved as tiff images and movies were made using QuickTime Player 7 Pro and compressed using Stomp (Shinywhitebox Ltd., Wellington, NZ). TomoX stacks of cell regions that had not been properly vitrified, recognised by the presence of segregation and aggregation patterns [20], were discarded.

2.7. Correlation between fluorescence and X-ray tomograms

Cryo-fluorescence images of RFP-Atg9 and GFP-LC3 signals were enlarged and overlaid onto images from the tomoX stacks using Adobe Photoshop. Several markers were used for alignment of the cryo-fluorescence data to the tomoX stack. The 250 nm gold fiducials could occasionally be detected in the green and red fluorescence channels, perhaps determined by cell and/ or ice thickness in that region. The regular array of the holes in the Quantifoil® grids could also be used for alignment in regions where the cells were thin or absent. Finally, the outline of the nucleus and plasma membrane also aided alignment in some regions. Candidate autophagosomes and Atg9-VTC, Quantifoil® holes and 250 nm gold fiducials; and neighbouring endosomes and endoplasmic reticulum were manually segmented and rendered in 3D using Amira software (Visage Imaging Inc.). The 3D

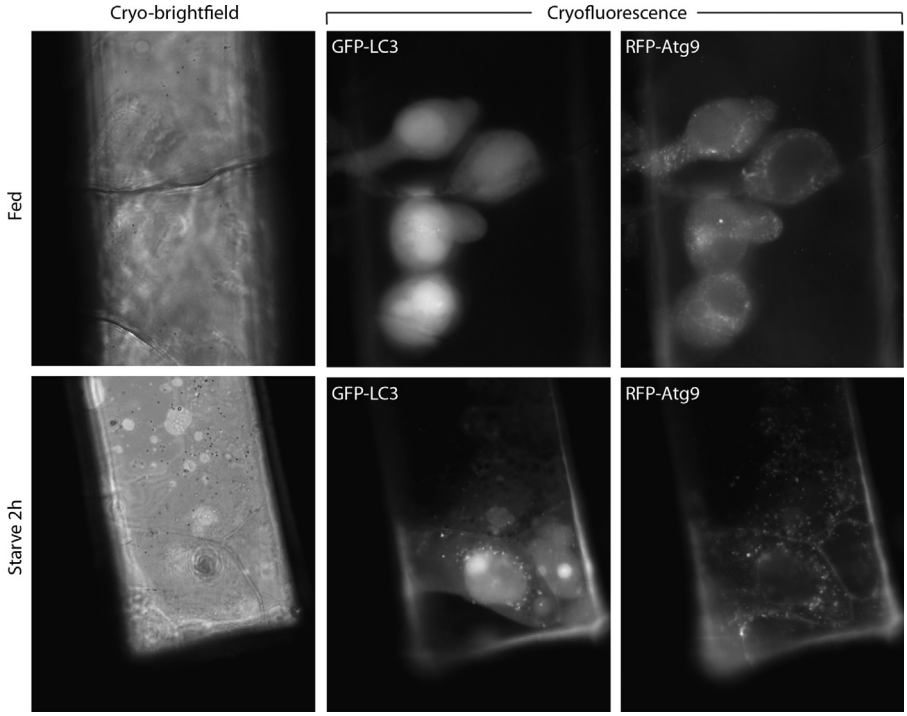

Fig. 2. Cryo-fluorescence microscopy of vitrified Hek293 cells co-expressing GFP-LC3 and RFP-Atg9. Cells in ice have a similar pattern of fluorescence expression to those imaged at room temperature. GFP-LC3 is mainly cytosolic under fed conditions but becomes punctate on recruitment to autophagosome membranes when the cells are starved. RFP-Atg9 is membrane-associated under both fed and starved conditions. Cells were selected for cryo-SXT based on morphology, distance from the grid bars, and quality of the ice.

model was then overlaid onto the cryo-fluorescence data to back-check the correlation.

3. Results

To investigate the formation of autophagosomes using cryo-SXT, Hek293 cells expressing GFP-LC3 and RFP-Atg9 were grown on HZB-2 grids (Fig. 1a) coated with holey-carbon foils in amino-acid starved conditions to induce autophagy. Cells were loaded with anti-TfnR-gold as a marker for the endocytic pathway, and plunge-frozen to preserve the cells within a thin layer of vitreous ice.

3.1. Cryo-fluorescence imaging of frozen-hydrated cells

The HZB cryo-SXT microscope has an associated in-line fluorescence microscope for localisation of cells immediately prior to X-ray imaging [19]. However, access to the cryo-SXT microscope is at a premium, so we introduced benchtop cryo-fluorescence microscopy [37] into our sample preparation workflow in the home laboratory in order to make best use of the time at the synchrotron beamline. Frozen grids were transferred to the cold stage of the cryo-fluorescence microscope under liquid nitrogen (Fig. 1b,c). The screening process also allowed us to check ice thickness and grid quality, which is especially important as cryo-preservation is one of the parameters associated with final tomogram quality [31]. Freezing artefacts including cracks and ice contamination could be easily identified (Fig. 1d,e).

Frozen cells co-expressing RFP-Atg9 and GFP-LC3 were selected, mapped and imaged (Fig. 2). As expected, GFP-LC3 is largely cytosolic under basal conditions, becoming punctate as it is recruited to autophagosomes during starvation; Atg9 is membrane-associated under both fed and starved conditions. Ice thickness could be assessed by the ability to focus the holes in the carbon film using cryo-brightfield imaging, or the GFP and RFP signals using cryo-fluorescence imaging. Thin ice led to disruption of cell morphology due to dehydration, whereas thick ice led to scattering of the signals and poorer focus. Regions of optimal ice thickness were selected (estimated at 5–8 μm). Thus entire grids or areas of grids unsuitable for imaging could be excluded from the X-ray data collection prior to arrival at the X-ray microscopy beamline.

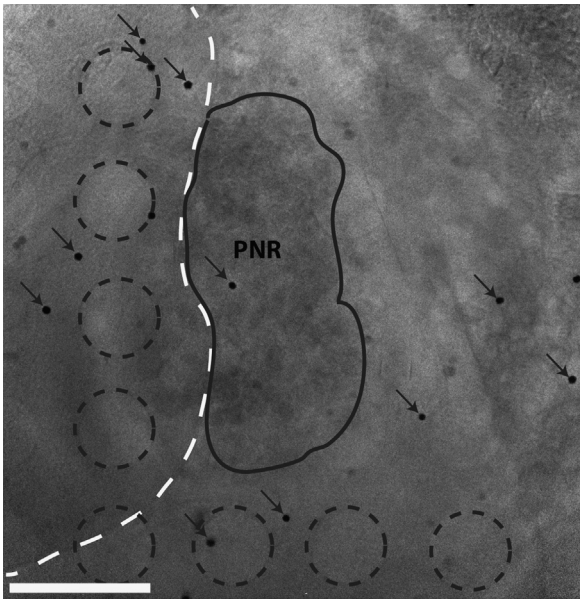

Fig. 3. 2D projection of a whole, frozen mammalian cell at 0° tilt imaged using cryo-SXT. The nuclear envelope is delineated with a dashed white line and the perinuclear region (PNR) containing the highest concentration of organelles is delineated with a black line. The holes of the Quantifoil® holey carbon film are circled. Alongside the 250 nm fiducials (arrows), the holes can be used to align cryo-fluorescence data with the soft X-ray tomogram. Scale bar: 5 μm.

3.2. Identifying endocytic compartments in cryo-SXT images using immunogold

Following cryo-fluorescence microscopy, grids were shipped to the HZB cryo full-field transmission X-ray microscope installed at the U41 beamline at the BESSY II electron storage ring (Berlin, Germany) for imaging at cryogenic temperatures [17]. A 2D projection through a whole frozen-hydrated cell is shown in Fig. 3. Even in the raw data, features including Quantifoil® holes (circles), 250 nm gold fiducials (arrows), the nuclear envelope

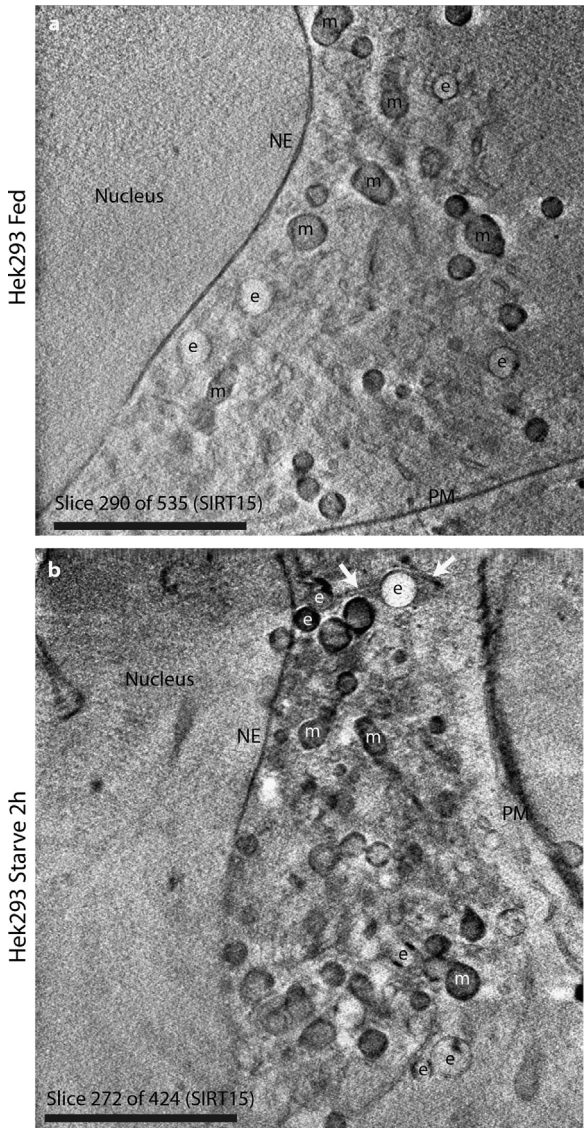

Fig. 4. Near-native state mammalian cell ultrastructure imaged using cryo-SXT. Fed (a) and starved (b) Hek293 cells were imaged using cryo-SXT and reconstructed using the SIRT algorithm in IMOD with 15 iterations. Structures including the nucleus, nuclear envelope (NE), endosomes (e), mitochondria (m) and plasma membrane (PM) can be identified by morphology alone. Endosomes (e) of the early endocytic and recycling pathways were identified by anti-TfnR-gold labelling. Tubules can be seen emanating from an endosome (white arrows). Scale bars: 5 μm.

(white line) and structures in the peri-nuclear region (PNR, black line) could be identified.

Raw tilt series from fed (Fig. 4a, Movie S1) and starved (Fig. 4b, Movies S3, S5) cells were reconstructed using IMOD [46] (Movie S2, S4, S6). The resolution of the data obtained using cryo-SXT is a function of the resolution of the zone plate objective, which collects the X-rays that have passed through the sample and images them on the CCD detector. Additionally, sample quality plays a pivotal role, as high-resolution data will never be obtainable from poorly prepared samples. In these experiments a 40 nm zone plate was used, which has a 3D resolution in the order of 40 nm^3 [20,33]. In terms of subcellular structure, the nucleus, the two bilayers of the nuclear envelope (NE), the plasma membrane (PM) and mitochondria (m) could be identified by morphology alone (Fig. 4). Putative endosomes (e) and tubular endosomes (white arrows, Fig. 4b) were also identified.

Supplementary material related to this article can be found online at http://dx.doi.org/10.1016/j.ultramic.2013.10.006.

We confirmed the identity of the putative endosomal structures in cryo-SXT images using an anti-TfnR-gold marker. Gold-containing endocytic structures could be divided into several distinct populations, having either X-ray lucent or X-ray dense lumens (Fig. 5). Though the diameter of individual gold particles (10 nm) was below the resolution of the microscope, clusters of endocytosed gold could easily be distinguished within spherical membrane-bound vacuoles (arrows) and vesicles (arrowhead). For each reconstruction (tomoX), both back projection (BP) and simultaneous iterative reconstruction technique (SIRT) algorithms were applied (Fig. 5a–c). Back projection reconstructions resulted in a lower signal-to-noise ratio but better resolution as assessed by the anti-TfnR-gold particles (arrows, Fig. 5a); SIRT reconstructions had a higher signal-to-noise ratio and increased contrast (Fig. 5b,c) resembling TEM images (Fig. 5d) but with lower resolution. For subsequent reconstructions, 15 SIRT iterations were used to give a balance between contrast and resolution.

3.3. Localisation of autophagosomes using cryo-CLXM

In initial analyses of tomograms, clear identification of the autophagosomal compartments was challenging therefore we moved to a correlative workflow. For cryo-CLXM, starved cells with co-localised RFP-Atg9 and GFP-LC3 (Fig. 6a) were re-located using the grid maps generated in the home laboratory and X-ray tilt series were collected (Movie S3). It was critical to relocate regions using the in-beamline fluorescence microscope first, as X-rays have been found to bleach the fluorescence signal [20]. Following reconstruction (Movie S4), several features were used to overlay the cryo-fluorescence images and tomoX stacks. The holes of the Quantifoil® film could be seen in cryo-brightfield, cryo-fluorescence and cryo-SXT images (raw and reconstructed) and so could be used as a marker for the overlays (Fig. 6b). In addition, some of the 250 nm gold fiducials were visible in all imaging modalities, and served to refine the alignment (white arrows, Fig. 6b). However, overlay accuracy was low due to the axial resolution of the fluorescence image compared with the axial resolution of each image from the tomoX stack. Nevertheless, extensive analysis of the tomoX stacks revealed structures resembling the lucent endosome-like organelles that are central to the Atg9-VTC (red arrowheads) [40] in close proximity to structures with lucent halos and dense cytosolic content characteristic of fully-formed autophagosomes (Fig. 6c, green arrowheads). The Atg9-VTC structures were located underneath the autophagosomes, occupying a depth of ~2.6 μm in a total cell depth of ~6.2 μm. Thus, it is possible that whilst the compartments appeared to be interacting by fluorescence microscopy because the signals coincided in the 2D projection image, the axial

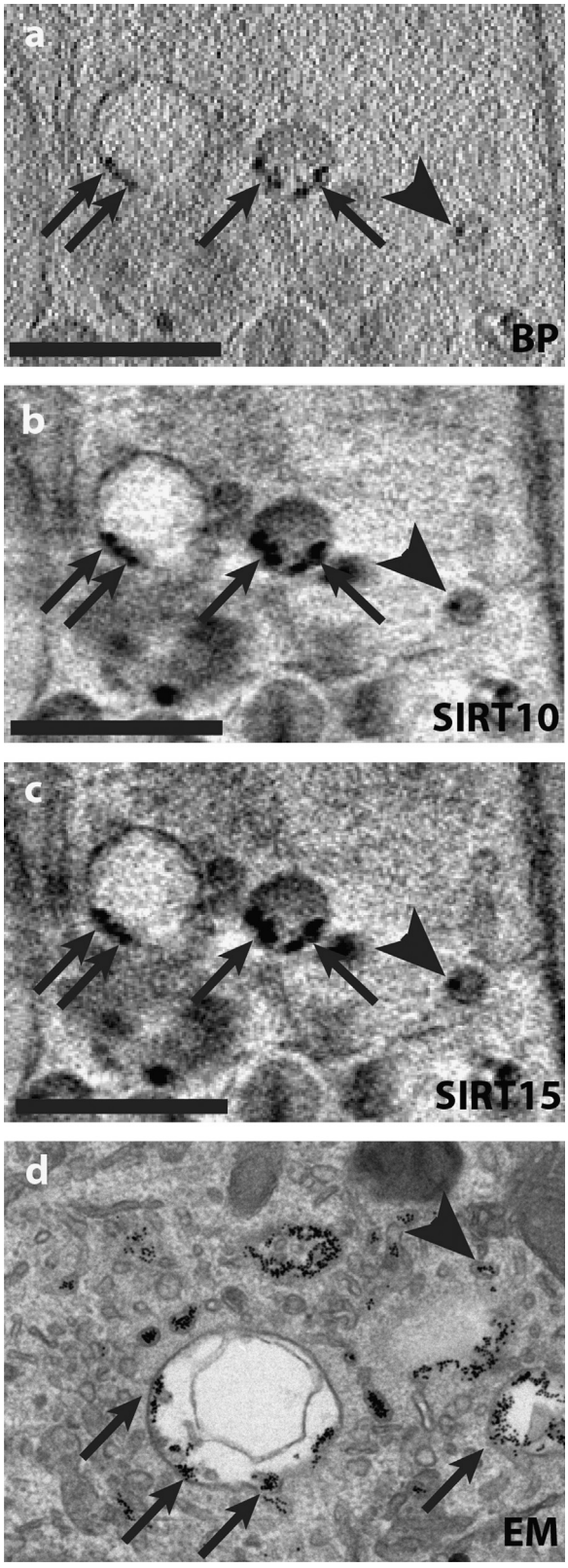

Fig. 5. Optimisation of data reconstruction and characterisation of endosomes. Endosomes exhibit both lucent and dense lumens in cryo-SXT images (a–c) and are spherical compared with the deformed membranes seen using chemical fixation and TEM (d). Arrows indicate anti-TfnR-10 nm gold particles in endosomes, arrowhead indicates gold particles in a trafficking vesicle. Comparison of tomogram reconstruction using back projection (BP) (a), SIRT with 10 iterations (SIRT10) (b) and SIRT with 15 iterations (SIRT15) (c) in IMOD. The back projection reconstruction gives better resolution of the gold particles but with a poorer signal-to-noise ratio. SIRT reconstruction gives slightly lower resolution, but better signal-to-noise, with contrast resembling that of electron microscopy (d). Scale bars: (a–c) 2 μm.

separation of the compartments as evidenced by the 3D X-ray data suggests that in reality they may not be close enough to interact.

3.4. Capturing autophagosome formation using cryo-CLXM

To increase the likelihood of capturing early autophagosomes, we performed correlative analysis of a cell where RFP-Atg9 and GFP-LC3 were co-localised in the same fluorescence focal plane. Cryo-SXT data was collected (Movie S5) and cryo-CLXM analysis performed as described in Section 3.3. Cryo-fluorescence (Fig. 7a) and cryo-SXT images (Movie S6) were overlaid to locate the underlying structure of co-localised RFP-Atg9 (red arrowheads) and GFP-LC3 (green arrowheads) (Fig. 7b). Structures were manually traced (segmented) in sequential tomoX images using Amira software (Visage Imaging Inc.) and rendered into a virtual model (Fig. 7c and Movie S7). 3D reconstructions of the Quantifoil™ holes and 250 nm gold fiducials (grey, Fig. 7c) were used for alignment of the model with the fluorescence data. Atg9-VTC (red), LC3-positive structures (green), anti-TfnR-gold loaded endosomes (yellow) and ER (blue) were segmented and rendered to aid 3D analysis of the organelles.

Supplementary material related to this article can be found online at http://dx.doi.org/10.1016/j.ultramic.2013.10.006.

Clusters of LC3-positive membranes were identified in several regions (Fig. 7 regions 1 and 2). The cup-shaped morphology of the LC3-positive membranes suggests that they represent omegasomes, which have been reported to emerge from PIP_3-rich subdomains of the ER [43,47]. Indeed, our images indicate extensive connections between the omegasomes and the endoplasmic reticulum in region 2. This pair of omegasomes (green arrowheads 1 and 2) was interconnected, suggesting that multiple omegasomes can arise from the same ER subdomain. ER membranes could not be unambiguously identified in region 1, possibly due to data reconstruction quality at the edges of the tomogram. Both pairs of omegasomes were closely associated with Atg9-VTC (red arrowheads) and clusters of TfnR-positive endosomes (yellow). The X-ray ultrastructure of endosomes (e) loaded with anti-TfnR-gold (black arrows) and omegasomes (green arrowheads) are shown in Fig. 7d. Virtual slices were selected from the tomoX stack in region 1 (slices 165, 180, 186, and 199) and region 2 (199, 204, and 235). Endosomes were spherical, with immunogold localised at the limiting membrane. Omegasomes appeared as cup-shaped membranes extending from the ER in close association with Atg9-VTC (green arrowheads, 1–4).

Finally, the most obvious difference between fed and starved cells was a change in the mitochondrial network (Fig. 8 and Movie S8). In some of the starved cells, fine connections could be seen to link

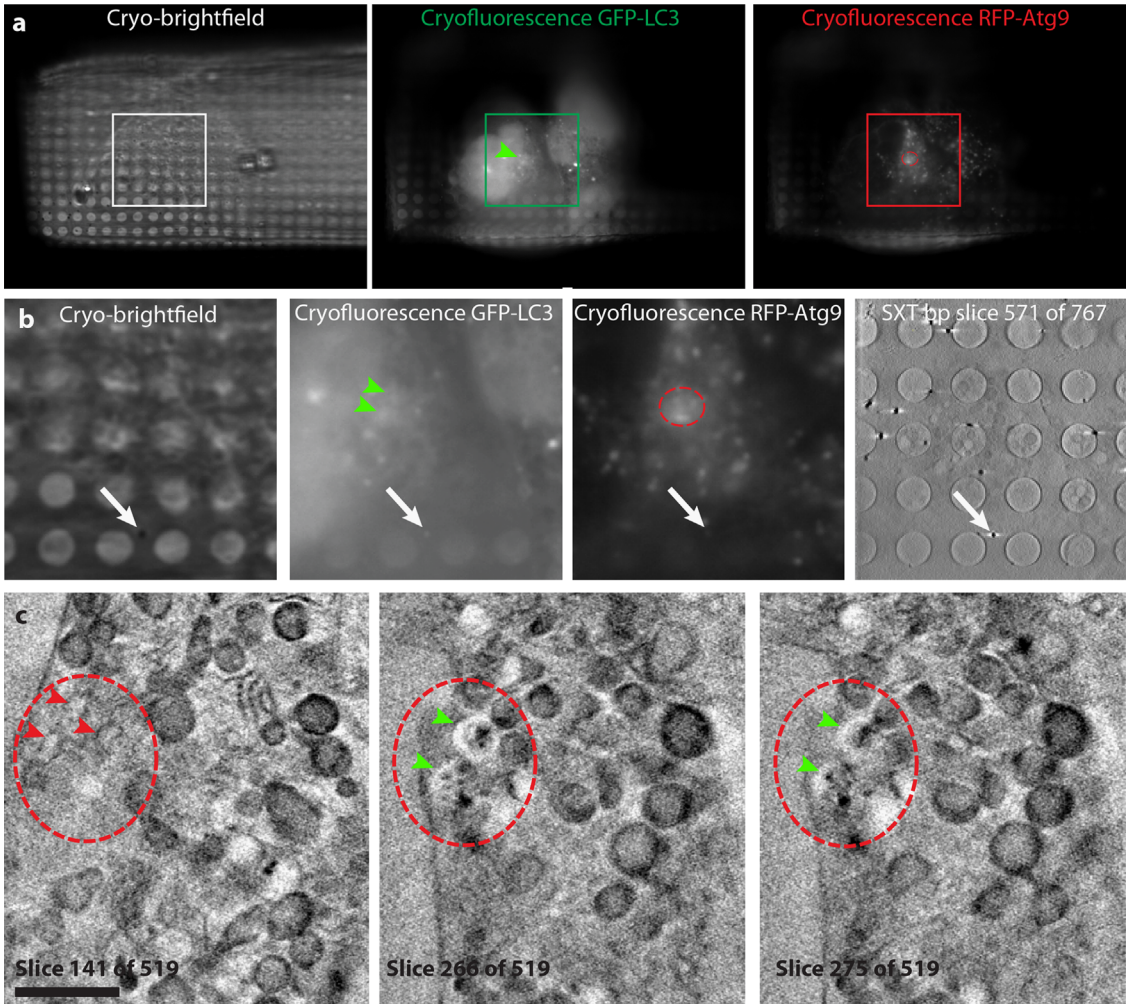

Fig. 6. Cryo-CLXM of autophagosomes in starved Hek293 cells. Cryo-fluorescence microscopy was used to identify and image a cell in which RFP-Atg9 and GFP-LC3 co-localised (a). The cell was relocated using the in-column fluorescence microscope on the U41-TXM beamline at the BESSY II synchrotron. A tilt series of $+55^\circ$ to -50° was collected and the tomogram reconstructed using IMOD. Quantifoil® holes, 250 nm gold fiducials and the cell nucleus were used to align the two datasets (b). Atg9-VTC membranes (red circle and arrowheads) were identified in close proximity to autophagosomes (green arrows), which had an X-ray-lucent region surrounding dense content (c), similar to autophagosome structure as seen by electron microscopy. Scale bars: 2 μm. (For interpretation of the references to colour in this figure legend, the reader is referred to the web version of this article.)

mitochondria over many microns (arrows), most easily visualised in 3D reconstructions of the data (yellow). Thus, the structure and relationships between organelles could be analysed over a depth of many microns, again highlighting the 3D imaging capabilities of cryo-SXT.

Supplementary material related to this article can be found online at http://dx.doi.org/10.1016/j.ultramic.2013.10.006.

4. Discussion

Cryo-SXT is the only imaging modality in which the ultrastructure of entire mammalian cells can be imaged in 'near-native' fully-hydrated state. The resolution is sufficient to detect subcellular organelles including the nucleus, the plasma membrane, the endoplasmic reticulum and mitochondria. Our study extends the organelles that can be recognised in cryo-SXT images to compartments of the endocytic and autophagy pathways.

Image formation in cryo-SXT is due to the natural contrast obtained when data are collected at an X-ray energy of ~510 eV, in the 'water window' between the K-absorption edges of carbon and oxygen. As expected, heavy metals in the form of gold nanoparticles were easily detected by their density, as previously reported for silver nanoparticles [30,48] and titanium dioxide nanoparticles [49]. Pre-loading of cells with an anti-TfnR-gold enabled unambiguous identification of early and recycling endosomes. This work could be extended in the future with gold conjugated to markers such as epidermal growth factor (EGF), to characterise the appearance of late endosomes and lysosomes. However, where organelles are inaccessible to externally-applied gold-conjugated markers, cryo-CLXM of cloned fluorophores is necessary for organelle identification and protein localisation.

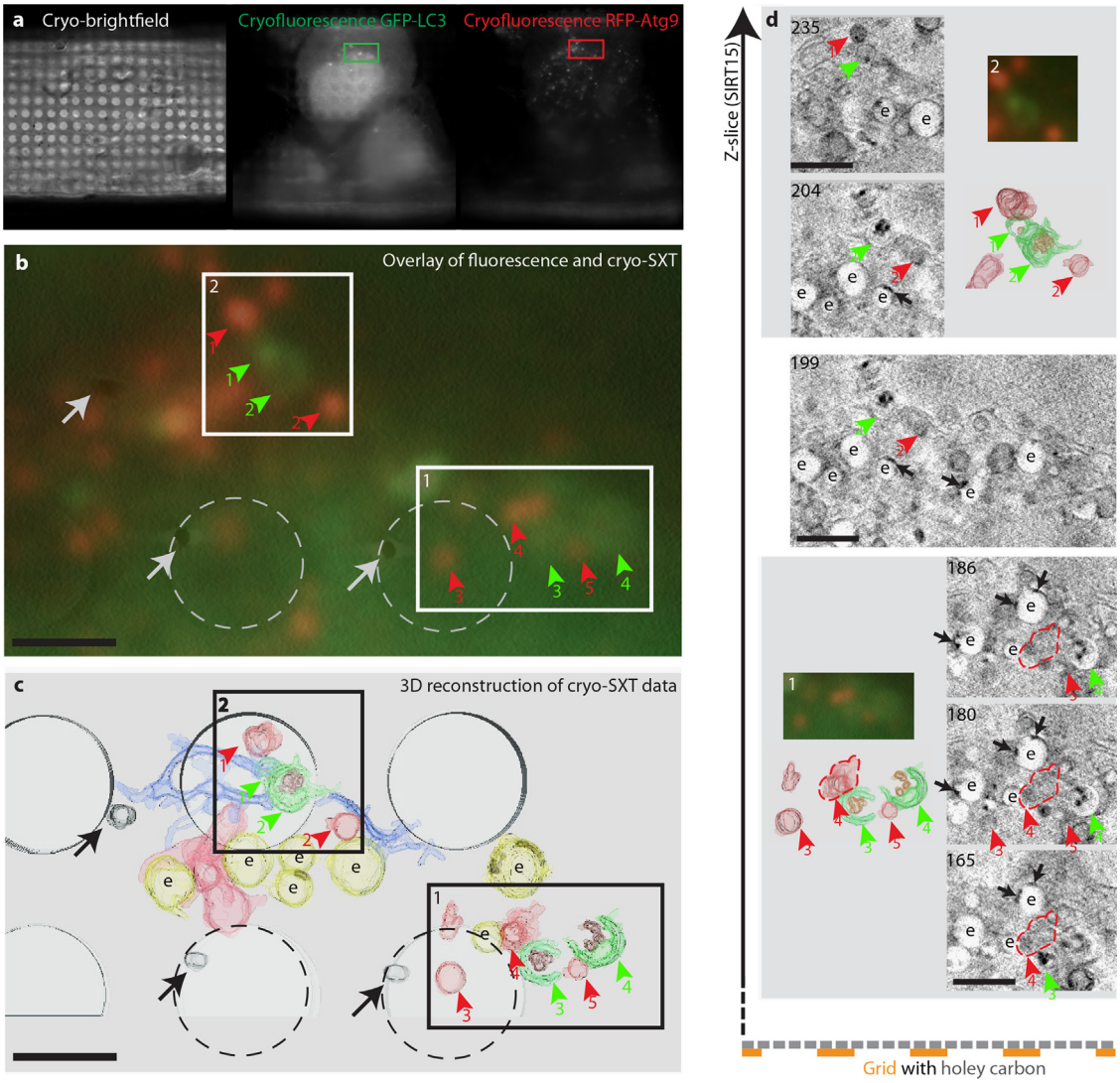

Fig. 7. Cryo-CLXM of omegasomes in starved Hek293 cells. (a) A cell in which RFP-Atg9 and GFP-LC3 co-localised in the same focal plane was identified and imaged as described in Fig. 6. Several regions (1 and 2) of RFP (red arrowheads) and GFP (green arrowheads) fluorescence were identified and overlaid onto the appropriate z-slice from the Quantifoil®/gold fiducial layer of the reconstructed tomoX stack (b). Features of interest, including Quantifoil® holes (grey), gold fiducials (dark grey), Atg9-VTC (red), LC3-positive omegasomes (green), endosomes (yellow) loaded with anti-TfnR-gold (black) and endoplasmic reticulum (blue) were manually segmented and rendered using Amira software (Visage Imaging Inc.) (c). (d) Structures from regions 1 and 2 were analysed in detail in the reconstructed tomoX stack. Six non-consecutive z-sections are shown, with numbers indicating the slice from the reconstruction (each having a thickness of approximately 15 nm). The slice at the bottom of the image is closest to the bottom of the cell and the carbon film. Region 1 contains two omegasomes (green arrowheads 3 and 4) with several Atg9-VTC (red arrowheads 3–5) either in direct contact with the omegasomes or endosomes (e) loaded with anti-TfnR-10 nm gold (black arrows). Region 2 contains two interconnected omegasomes (green arrowheads 1 and 2), connected to the endoplasmic reticulum and in close contact with Atg9-VTCs (red arrowheads 1 and 2). Scale bars: 2 μm. (For interpretation of the references to colour in this figure legend, the reader is referred to the web version of this article.)

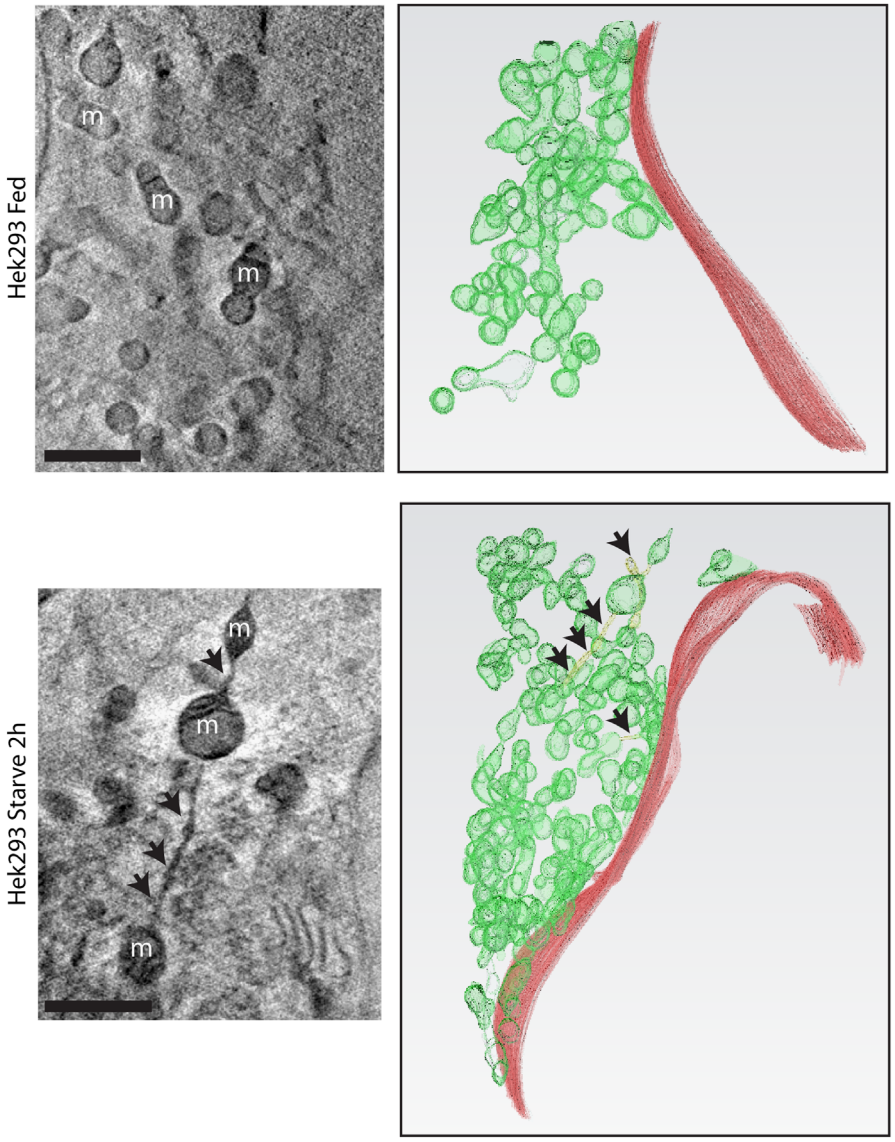

Fig. 8. Tubulation of mitochondrial networks under starvation conditions. Z-slices from the tomoX stack and 3D rendering of mitochondria (m; green) in relation to the nuclear envelope (red) are shown from fed and starved Hek293 cells. Large structures such as mitochondria can be followed through the volume of the tomoX stacks, and demonstrate connections (black arrows, rendered in yellow) that are rarely seen in resin-embedded TEM samples. Scale bars: 2 μm. (For interpretation of the references to colour in this figure legend, the reader is referred to the web version of this article.)

A major advantage of using the cryo-fluorescence stage in the cryo-CLXM workflow (rather than a cryogenic light microscope or a fluorescence microscope inside the X-ray microscope) is that grids can be screened for quality and protein localisation in the home laboratory before travelling to the synchrotron, enabling efficient use of beamtime. In addition, the cryo-fluorescence stage can be retro-fitted onto any widefield epifluorescence microscope, which will help to make the technique accessible to research laboratories without access to advanced imaging expertise. As previously reported, fluorophores are preserved and stabilised by vitrification [50]. In this study, regions where RFP-Atg9 and GFP-LC3 co-localised could be selected with certainty that membranes would not alter prior to X-ray imaging. In the future, a combination of live-cell imaging immediately followed by plunge-freezing would add a fourth dimension to the data.

Cryo-SXT ultrastructure was similar to that seen in cells prepared by either HPF and freeze substitution into resin for ambient temperature TEM, or plunge-freezing for cryo-TEM. Distortions of membranes caused by shrinkage during traditional chemical fixation and resin-embedding for TEM were absent. A major difference between EM and cryo-SXT images is the contrast mechanism. Whereas heavy metals are required to produce contrast in routine TEM and techniques like particle averaging are required to generate good contrast in cryo-TEM, cryo-SXT detects the inherent contrast of the biological material and the resulting images have high natural contrast. Nevertheless, cryo-SXT does not currently challenge TEM for resolution, and so the techniques are complementary, extracting different information from the sample.

The extended penetration depth of the X-rays (compared to electrons) allows data to be collected on whole cells, enabling 3D imaging of intact cellular structures and analysis of connected networks within the cell. We applied cryo-SXT to whole mammalian cells undergoing starvation. The most obvious structural effect of starvation was the tubulation of mitochondria. As previously reported, mitochondria can supply membranes for autophagy under extreme starvation conditions [51] and can also become tubulated and form extensive networks, protecting themselves from autophagosomal degradation [52,53]. To investigate further the mitochondrial link to early autophagy, we plan to label live

cells with mito-tracker and induce autophagy to study time-dependent interactions using cryo-SXT.

The extended penetration depth of the X-rays also allowed us to image clusters of endosomes and autophagosomes through continuous aligned image stacks. We were able to identify multiple omegasomes arising from the 'hot-spots' on the endoplasmic reticulum, which supports and extends TEM tomography studies that showed connections between phagophores and the ER [54]. Importantly, we have not seen similar structures in our previous TEM or CLEM work, where early autophagosomal structures were elusive, suggesting that these structures may only be seen by cryo-preparation and cryo-imaging. We anticipate that cryo-SXT will benefit studies of other structures that are poorly preserved by chemical fixation, including cytoskeletal elements and clathrin-coated vesicles, as well as larger organelles such as Weibel–Palade Bodies and mitochondria.

In summary, the combination of cryo-preparation, cryo-fluorescence microscopy and cryo-SXT has wide application for imaging cellular structures as close to native-state as possible, and is particularly effective in capturing dynamic membrane trafficking processes that are poorly preserved using standard EM techniques. Cryo-SXT does not replace light or electron microscopy, but rather fills a 'sample volume vs. resolution gap' between light microscopes (that can image whole cells but with limited resolution) and transmission electron microscopes (that can image at nanometre resolution but only through thin sections of cells). From the data obtained in this proof-of-concept study, it is clear that there are advantages to cryo-CLXM imaging for wider cell biological applications.

5. Conclusions

Cryo-SXT minimises sample processing artefacts and gives unparalleled views of native-state cellular ultrastructure in three dimensions. Cryo-CLXM will be widely applicable to structure/function studies in cell biology. This technique can be exploited generically for non-invasive imaging, giving new insights into cells through simultaneous analysis of morphology, protein localisation and atomic composition.

Acknowledgements

We thank Prof. Clare Futter for the anti-TfnR-gold, Linkam Scientific Instruments for modifications to the cryo-fluorescence stage and Prof. Banafshe Larijani for critical reading of the manuscript. We thank HZB for the allocation of synchrotron radiation beamtime. The research leading to these results has received funding from the European Community's Seventh Framework Programme (FP7/2007–2013) under BioStruct-X (Grant Agreement no. 283570). LMC, AW, MR and SAT are grateful for support from Cancer Research UK.

References

[1] R.S. Polishchuk, E.V. Polishchuk, P. Marra, S. Alberti, R. Buccione, A. Luini, A. A. Mironov, Correlative light-electron microscopy reveals the tubular–saccular ultrastructure of carriers operating between golgi apparatus and plasma membrane, J. Cell. Biol. 148 (2000) 45–58.

[2] E. Brown, J. Mantell, D. Carter, G. Tilly, P. Verkade, Studying intracellular transport using high-pressure freezing and correlative light electron microscopy, Semin. Cell. Dev. Biol. 20 (2009) 910–919.

[3] N.A. Bright, M.J. Gratian, J.P. Luzio, Endocytic delivery to lysosomes mediated by concurrent fusion and kissing events in living cells, Curr. Biol.: CB 15 (2005) 360–365.

[4] R.S. Polishchuk, E. San Pietro, A. Di Pentima, S. Tete, J.S. Bonifacino, Ultrastructure of long-range transport carriers moving from the trans Golgi network to peripheral endosomes, Traffic (Cph., Den.) 7 (2006) 1092–1103.

[5] K.J. Darcy, K. Staras, L.M. Collinson, Y. Goda, Constitutive sharing of recycling synaptic vesicles between presynaptic boutons, Nat. Neurosci. 9 (2006) 315–321.

[6] E.A. Bouwens, M.J. Mourik, M. van den Biggelaar, J.C. Eikenboom, J. Voorberg, K.M. Valentijn, K. Mertens, Factor VIII alters tubular organization and functional properties of von Willebrand factor stored in Weibel–Palade bodies, Blood 118 (2011) 5947–5956.

[7] G. Perinetti, T. Muller, A. Spaar, R. Polishchuk, A. Luini, A. Egner, Correlation of 4Pi and electron microscopy to study transport through single Golgi stacks in living cells with super resolution, Traffic (Cph., Den.) 10 (2009) 379–391.

[8] A.A. Mironov, A.A. Mironov Jr., G.V. Beznoussenko, A. Trucco, P. Lupetti, J.D. Smith, W.J. Geerts, A.J. Koster, K.N. Burger, M.E. Martone, T.J. Deerinck, M.H. Ellisman, A. Luini, ER-to-Golgi carriers arise through direct en bloc protrusion and multistage maturation of specialized ER exit domains, Dev. Cell 5 (2003) 583–594.

[9] H.H. Hanson, S. Kang, M. Fernandez-Monreal, T. Oung, M. Yildirim, R. Lee, K. Suyama, R.B. Hazan, G.R. Phillips, LC3-dependent intracellular membrane tubules induced by gamma-protocadherins A3 and B2: a role for intraluminal interactions, J. Biol. Chem. 285 (2010) 20982–20992.

[10] A. Orsi, M. Razi, H. Dooley, D. Robinson, A. Weston, L. Collinson, S. Tooze, Dynamic and transient interactions of Atg9 with autophagosomes, but not membrane integration, is required for autophagy, Mol. Biol. Cell (2012).

[11] M. Razi, S.A. Tooze, Correlative light and electron microscopy, Methods Enzymol. 452 (2009) 261–275.

[12] J.A. Berriman, S. Li, L.J. Hewlett, S. Wasilewski, F.N. Kiskin, T. Carter, M.J. Hannah, P.B. Rosenthal, Structural organization of Weibel–Palade bodies revealed by cryo-EM of vitrified endothelial cells, Proc. Natl. Acad. Sci. U.S.A. 106 (2009) 17407–17412.

[13] A. Al-Amoudi, L.P. Norlen, J. Dubochet, Cryo-electron microscopy of vitreous sections of native biological cells and tissues, J. Struct. Biol. 148 (2004) 131–135.

[14] A. Rigort, F.J. Bauerlein, E. Villa, M. Eibauer, T. Laugks, W. Baumeister, J.M. Plitzko, Focused ion beam micromachining of eukaryotic cells for cryoelectron tomography, Proc. Natl. Acad. Sci. U.S.A. 109 (2012) 4449–4454.

[15] C.A. Larabell, K.A. Nugent, Imaging cellular architecture with X-rays, Curr. Opin. Struct. Biol. 20 (2010) 623–631.

[16] D.Y. Parkinson, L.R. Epperly, G. McDermott, M.A. Le Gros, R.M. Boudreau, C.A. Larabell, Nanoimaging cells using soft X-ray tomography, Methods Mol. Biol. (Clifton, N.J.) 950 (2013) 457–481.

[17] G. Schneider, P. Guttmann, S. Heim, S. Rehbein, F. Mueller, K. Nagashima, J.B. Heymann, W.G. Muller, J.G. McNally, Three-dimensional cellular ultrastructure resolved by X-ray microscopy, Nat. Methods 7 (2010) 985–987.

[18] M.A. Le Gros, G. McDermott, C.A. Larabell, X-ray tomography of whole cells, Curr. Opin. Struct. Biol. 15 (2005) 593–600.

[19] G. Schneider, P. Guttmann, S. Rehbein, S. Werner, R. Follath, Cryo X-ray microscope with flat sample geometry for correlative fluorescence and nanoscale tomographic imaging, J. Struct. Biol. 177 (2012) 212–223.

[20] C. Hagen, P. Guttmann, B. Klupp, S. Werner, S. Rehbein, T.C. Mettenleiter, G. Schneider, K. Grunewald, Correlative VIS–fluorescence and soft X-ray cryo-microscopy/tomography of adherent cells, J. Struct. Biol. 177 (2012) 193–201.

[21] A. Weiner, S. Kapishnikov, E. Shimoni, S. Cordes, P. Guttmann, G. Schneider, M. Elbaum, Vitrification of thick samples for soft X-ray cryo-tomography by high pressure freezing, J. Struct. Biol. 181 (2013) 77–81.

[22] G. Schmahl, D. Rudolph, B. Niemann, P. Guttmann, J. Thieme, G. Schneider, C. David, M. Diehl, T. Wilhein, X-ray microscopy studies, Optik 93 (1993) 95–102.

[23] J. Kirz, C. Jacobsen, M. Howells, Soft X-ray microscopes and their biological applications, Q. Rev. Biophys. 28 (1995) 33–130.

[24] W. Gu, L.D. Etkin, M.A. Le Gros, C.A. Larabell, X-ray tomography of *Schizosaccharomyces pombe*, Differentiation. 75 (2007) 529–535.

[25] C.A. Larabell, M.A. Le Gros, X-ray tomography generates 3-D reconstructions of the yeast, *Saccharomyces cerevisiae*, at 60-nm resolution, Mol. Biol. Cell. 15 (2004) 957–962.

[26] D.Y. Parkinson, G. McDermott, L.D. Etkin, M.A. Le Gros, C.A. Larabell, Quantitative 3-D imaging of eukaryotic cells using soft X-ray tomography, J. Struct. Biol. 162 (2008) 380–386.

[27] M. Uchida, G. McDermott, M. Wetzler, M.A. Le Gros, M. Myllys, C. Knoechel, A.E. Barron, C.A. Larabell, Soft X-ray tomography of phenotypic switching and the cellular response to antifungal peptoids in *Candida albicans*, Proc. Natl. Acad. Sci. U.S.A. 106 (2009) 19375–19380.

[28] M. Uchida, Y. Sun, G. McDermott, C. Knoechel, M.A. Le Gros, D. Parkinson, D.G. Drubin, C.A. Larabell, Quantitative analysis of yeast internal architecture using soft X-ray tomography, Yeast (Chichester, Engl.) 28 (2011) 227–236.

[29] E.J. Clowney, M.A. LeGros, C.P. Mosley, F.G. Clowney, E.C. Markenskoff-Papadimitriou, M. Myllys, G. Barnea, C.A. Larabell, S. Lomvardas, Nuclear aggregation of olfactory receptor genes governs their monogenic expression, Cell 151 (2012) 724–737.

[30] W. Meyer-Ilse, D. Hamamoto, A. Nair, S.A. Lelievre, G. Denbeaux, L. Johnson, A.L. Pearson, D. Yager, M.A. Legros, C.A. Larabell, High resolution protein localization using soft X-ray microscopy, J. Microsc. 201 (2001) 395–403.

[31] W.G. Muller, J.B. Heymann, K. Nagashima, P. Guttmann, S. Werner, S. Rehbein, G. Schneider, J.G. McNally, Towards an atlas of mammalian cell ultrastructure by cryo soft X-ray tomography, J. Struct. Biol. 177 (2012) 179–192.

[32] J.L. Carrascosa, F.J. Chichon, E. Pereiro, M.J. Rodriguez, J.J. Fernandez, M. Esteban, S. Heim, P. Guttmann, G. Schneider, Cryo-X-ray tomography of

vaccinia virus membranes and inner compartments, J. Struct. Biol. 168 (2009) 234–239.
[33] F.J. Chichon, M.J. Rodriguez, E. Pereiro, M. Chiappi, B. Perdiguero, P. Guttmann, S. Werner, S. Rehbein, G. Schneider, M. Esteban, J.L. Carrascosa, Cryo X-ray nano-tomography of vaccinia virus infected cells, J. Struct. Biol. 177 (2012) 202–211.
[34] M.A. Le Gros, G. McDermott, M. Uchida, C.G. Knoechel, C.A. Larabell, High-aperture cryogenic light microscopy, J. Microsc. 235 (2009) 1–8.
[35] G. McDermott, M.A. Le Gros, C.G. Knoechel, M. Uchida, C.A. Larabell, Soft X-ray tomography and cryogenic light microscopy: the cool combination in cellular imaging, Trends Cell Biol. 19 (2009) 587–595.
[36] G. McDermott, M.A. Le Gros, C.A. Larabell, Visualizing cell architecture and molecular location using soft x-ray tomography and correlated cryo-light microscopy, Annu. Rev. Phys. Chem. 63 (2012) 225–239.
[37] L.F. van Driel, J.A. Valentijn, K.M. Valentijn, R.I. Koning, A.J. Koster, Tools for correlative cryo-fluorescence microscopy and cryo-electron tomography applied to whole mitochondria in human endothelial cells, Eur. J. Cell. Biol. 88 (2009) 669–684.
[38] E.L. Eskelinen, To be or not to be? Examples of incorrect identification of autophagic compartments in conventional transmission electron microscopy of mammalian cells, Autophagy 4 (2008) 257–260.
[39] E.L. Eskelinen, A.L. Kovacs, Double membranes vs. lipid bilayers, and their significance for correct identification of macroautophagic structures, Autophagy 7 (2011) 931–932.
[40] A. Orsi, H.E. Polson, S.A. Tooze, Membrane trafficking events that partake in autophagy, Curr. Opin. Cell Biol. 22 (2010) 150–156.
[41] F. Reggiori, S.A. Tooze, Autophagy regulation through Atg9 traffic, J. Cell. Biol. 198 (2012) 151–153.
[42] K.T. Tokuyasu, A technique for ultracryotomy of cell suspensions and tissues, J. Cell Biol. 57 (1973) 551–565.
[43] E.L. Axe, S.A. Walker, M. Manifava, P. Chandra, H.L. Roderick, A. Habermann, G. Griffiths, N.T. Ktistakis, Autophagosome formation from membrane compartments enriched in phosphatidylinositol 3-phosphate and dynamically connected to the endoplasmic reticulum, J. Cell Biol. 182 (2008) 685–701.
[44] E.Y. Chan, S. Kir, S.A. Tooze, siRNA screening of the kinome identifies ULK1 as a multidomain modulator of autophagy, J. Biol. Chem. 282 (2007) 25464–25474.
[45] R. Kochl, X.W. Hu, E.Y. Chan, S.A. Tooze, Microtubules facilitate autophagosome formation and fusion of autophagosomes with endosomes, Traffic (Cph., Den.) 7 (2006) 129–145.
[46] J.R. Kremer, D.N. Mastronarde, J.R. McIntosh, Computer visualization of three-dimensional image data using IMOD, J. Struct. Biol. 116 (1996) 71–76.
[47] M. Hayashi-Nishino, N. Fujita, T. Noda, A. Yamaguchi, T. Yoshimori, A. Yamamoto, A subdomain of the endoplasmic reticulum forms a cradle for autophagosome formation, Nat. Cell. Biol. 11 (2009) 1433–1437.
[48] D. Drescher, P. Guttmann, T. Buchner, S. Werner, G. Laube, A. Hornemann, B. Tarek, G. Schneider, J. Kneipp, Specific biomolecule corona is associated with ring-shaped organization of silver nanoparticles in cells, Nanoscale 5 (2013) 9193–9198.
[49] J.M. Ashcroft, W. Gu, T. Zhang, S.M. Hughes, K.B. Hartman, C. Hofmann, A.G. Kanaras, D.A. Kilcoyne, M. Le Gros, Y. Yin, A.P. Alivisatos, C.A. Larabell, TiO2 nanoparticles as a soft X-ray molecular probe, Chem. Commun. (Camb.e, Engl.) (2008) 2471–2473.
[50] C.L. Schwartz, V.I. Sarbash, F.I. Ataullakhanov, J.R. McIntosh, D. Nicastro, Cryo-fluorescence microscopy facilitates correlations between light and cryo-electron microscopy and reduces the rate of photobleaching, J. Microsc. 227 (2007) 98–109.
[51] D.W. Hailey, A.S. Rambold, P. Satpute-Krishnan, K. Mitra, R. Sougrat, P.K. Kim, J. Lippincott-Schwartz, Mitochondria supply membranes for autophagosome biogenesis during starvation, Cell 141 (2010) 656–667.
[52] L.C. Gomes, G.D. Benedetto, L. Scorrano, During autophagy mitochondria elongate, are spared from degradation and sustain cell viability, Nat. Cell Biol. 13 (2011) 589–598.
[53] A.S. Rambold, B. Kostelecky, N. Elia, J. Lippincott-Schwartz, Tubular network formation protects mitochondria from autophagosomal degradation during nutrient starvation, Proc. Natl. Acad. Sci. U.S.A. 108 (2011) 10190–10195.
[54] P. Yla-Anttila, H. Vihinen, E. Jokitalo, E.L. Eskelinen, 3D tomography reveals connections between the phagophore and endoplasmic reticulum, Autophagy 5 (2009) 1180–1185.